

Non-thermal emission from mildly relativistic dynamical ejecta of neutron star mergers

Gilad Sadeh^{*}, Or Guttman, Eli Waxman

Dept. of Particle Phys. & Astrophys., Weizmann Institute of Science, Rehovot 76100, Israel

Accepted XXX. Received YYY; in original form ZZZ

ABSTRACT

Binary neutron star mergers are expected to produce fast dynamical ejecta, with mildly relativistic velocities extending to $\beta = v/c > 0.6$. We consider the radio to X-ray synchrotron emission produced by collisionless shocks driven by such fast ejecta into the interstellar medium. Analytic expressions are given for spherical ejecta with broken power-law mass (or energy) distributions, $M(> \gamma\beta) \propto (\gamma\beta)^{-s}$ with $s = s_{\text{KN}}$ at $\gamma\beta < \gamma_0\beta_0$ and $s = s_{\text{ft}}$ at $\gamma\beta > \gamma_0\beta_0$ (where γ is the Lorentz factor). For parameter values characteristic of merger calculation results- a "shallow" mass distribution, $1 < s_{\text{KN}} < 3$, for the bulk of the ejecta (at $\gamma\beta \approx 0.2$), and a steep, $s_{\text{ft}} > 5$, "fast tail" mass distribution- our model provides an accurate (to 10's of percent) description of the evolution of the flux, including at the phase of deceleration to sub-relativistic expansion. This is a significant improvement over earlier results, based on extrapolations of results valid for $\gamma\beta \gg 1$ or $\ll 1$ to $\gamma\beta \approx 1$, which overestimate the flux by an order of magnitude for typical parameter values. It will enable a more reliable inference of ejecta parameters from future measurements of the non-thermal emission. For the merger event GW170817, the existence of a "fast tail" is expected to produce detectable radio and X-ray fluxes over a time scale of $\sim 10^4$ days.

Key words: gravitational waves – stars: neutron – neutron star mergers

1 INTRODUCTION

Mergers of binary neutron stars (BNS) are expected to produce ejecta expanding at mildly relativistic velocities, $\gamma\beta > 0.1$, through several different mechanisms including dynamic ejection by tidal interaction and shocks, neutrino driven winds and (secular, spiral wave) mass ejection from a disk formed during the merger (see Fernández & Metzger 2016; Radice et al. 2020, for reviews). The amount of ejected mass and its velocity distribution depend on the parameters of the merging system and on the equation of state (EoS) of the nuclear matter. Measurements of the electromagnetic emission generated by the expanding ejecta will enable us to constrain its properties, and hence the parameters of the merging binary and of the EoS.

Observations of the optical (UV-IR) electromagnetic counterpart of GW170817 are consistent with an ejecta of $\approx 0.05M_{\odot}$ expanding at $\beta > 0.1$ and undergoing continuous heating by radioactive decays (Arcavi et al. 2017; Nicholl et al. 2017; Metzger 2017). This is remarkably consistent with the "kilonova" emission predicted to follow NS mergers (Li & Paczyński 1998). However, the detailed properties of the ejecta, that are inferred from observations, are inconsistent with those obtained in merger simulations (see e.g. Nedora et al. 2021b, for a recent detailed discussion). In particular, the mass of the ejecta is larger than obtained in simulations, and it is difficult to explain the existence of a fairly massive, $\approx 0.05M_{\odot}$, fast, $v \sim 0.3c$, component with low opacity corresponding to a large initial electron fraction

Y_e , that is suggested by the early UV/blue emission (Waxman et al. 2018).

Numeric merger calculations find that the velocity distribution of the dynamical ejecta may extend to large velocities, well above the characteristic velocity, $\beta \sim 0.1 - 0.2$, of the bulk of the ejecta that is responsible for the generation of the UV-IR "kilonova" (KN) emission (e.g. Bauswein et al. 2013; Ishii et al. 2018; Radice et al. 2018; Shibata & Hotokezaka 2019; Ciolfi & Kalinani 2020; Bernuzzi et al. 2020; Nedora et al. 2021a; Dean et al. 2021; Hajela et al. 2022). The existence of such a fast ejecta "tail" has recently been suggested as an explanation of a possible "re-brightening" of the X-ray emission of the GW170817 electromagnetic counterpart (Nedora et al. 2021a; Hajela et al. 2022). However, the evidence for rebrightening is not conclusive (Balasubramanian et al. 2021, 2022; Troja et al. 2022; O'Connor & Troja 2022). The mass and velocity profile of the "fast tail" depend strongly on the parameters of the binary system and on the EoS. Depending on parameter values, the ejecta mass at $\beta > 0.6$ varies, for example, between $10^{-7}M_{\odot}$ and $10^{-4}M_{\odot}$, and the maximal velocity varies from $\gamma\beta \approx 0.6$ to $\gamma\beta > 3$. This implies that measurements of the non-thermal emission driven by the fast ejecta may provide stringent constraints on model parameters.

Two points should, however, be noted here. First, a reliable determination of constraints would require a significant reduction of the current large numerical uncertainty in the numerically calculated fast tail parameters, as reflected by the large variations of results between different simulations (e.g. Dean et al. 2021). Second, if BNS mergers are the sources of (short) gamma-ray bursts (see Mészáros 2002; Piran 2004; Nakar 2007, for reviews), then they are expected to launch highly relativistic jets. Depending on the jet axis with respect

* E-mail: gilad.sade@weizmann.ac.il

to our line of sight, and on the ratio of energies carried by the jet and by the dynamical ejecta, the emission of non-thermal radiation driven by the jet may dominate that driven by the dynamical ejecta. In the case of GW170817, the rapid decline of the observed non-thermal emission (Troja et al. 2019; Fong et al. 2019; Lamb et al. 2019; Hajela et al. 2019; Troja et al. 2020; Makhathini et al. 2020; Nakar & Piran 2020) and the super-luminal motion of the radio centroid suggest that the observed non-thermal emission is driven by a relativistic jet (the presence of plasma expanding at $\gamma > 10$ cannot be directly inferred from observations, which may be accounted for by a $\gamma \sim 4$ jet Mooley et al. 2018). In general, due to the lower mass and higher Lorentz factor of the jet, we may expect the emission to be dominated at late time by the dynamical ejecta. The interpretation of future observations will require disentangling the two components.

We consider in this paper the radio to X-ray synchrotron emission produced by collisionless shocks driven by mildly relativistic ejecta expanding into an interstellar medium (ISM) with a uniform (number) density n . Analytic expressions are derived for the case of spherical ejecta (the effects of deviations from spherical symmetry will be discussed in a follow-up paper) with a broken power-law dependence of mass on momentum,

$$M(> \gamma\beta) = M_0 \begin{cases} \left(\frac{\gamma\beta}{\gamma_0\beta_0}\right)^{-s_{\text{ft}}} & \text{for } \gamma_0\beta_0 < \gamma\beta, \\ \left(\frac{\gamma\beta}{\gamma_0\beta_0}\right)^{-s_{\text{KN}}} & \text{for } 0.1 < \gamma\beta < \gamma_0\beta_0, \end{cases} \quad (1)$$

with parameter values characteristic of the results of numerical calculations of the dynamical ejecta (e.g. Radice et al. 2018; Hajela et al. 2022; Nedora et al. 2021a; Fujibayashi et al. 2022; Rosswog et al. 2022)- a "shallow" mass distribution, $1 < s_{\text{KN}} < 3$, for the bulk of the mass (at $\gamma\beta \approx 0.2$) and a steep, $s_{\text{ft}} > 5$, fast tail mass distribution (see, e.g. figure 10 of Hajela et al. 2022, for a useful description of mass profiles obtained in various calculations). We note that the "shallow" dependence of mass on velocity at $\gamma\beta < 0.3$ is consistent with the early evolution of the photospheric radius of the emission following GW170817, which implies $M(> \gamma\beta) \propto (\gamma\beta)^{-s_{\text{KN}}}$ with $s_{\text{KN}} \approx 1.6$ at $0.1 < \gamma\beta < 0.3$ (Waxman et al. 2018). Analytic expressions for a broken power-law dependence of ejecta energy on momentum,

$$E(> \gamma\beta) = E_0 \begin{cases} \left(\frac{\gamma\beta}{\gamma_0\beta_0}\right)^{-\alpha_{\text{ft}}} & \text{for } \gamma_0\beta_0 < \gamma\beta, \\ \left(\frac{\gamma\beta}{\gamma_0\beta_0}\right)^{-\alpha_{\text{KN}}} & \text{for } 0.1 < \gamma\beta < \gamma_0\beta_0, \end{cases} \quad (2)$$

are also provided ($\alpha_{\text{ft}} > 3, 0 < \alpha_{\text{KN}} < 1.5$), based on the results obtained for a broken power-law dependence of mass on momentum.

The non-thermal flux is derived assuming that fractions ε_e and ε_B of the post-shock internal energy density are carried by non-thermal electrons and magnetic fields respectively, and the electrons are assumed to follow a power-law energy distribution, $dn_e/d\gamma_e \propto \gamma_e^{-p}$, where γ_e is the electron Lorentz factor (at the plasma rest-frame) and $2 \leq p \leq 2.5$. This phenomenological description of the post-shock plasma conditions is supported by a wide range of observations and plasma calculations, for both relativistic and non-relativistic shocks (see Blandford & Eichler 1987; Waxman 2006; Bykov & Treumann 2011; Sironi et al. 2013, for reviews).

The accuracy of the analytic approximations derived in this paper for the non-thermal flux is verified through comparison to numerical calculations for a wide range of parameter values. It is significantly improved compared to that of earlier work, mainly due to an improved treatment of the dynamics of the ejecta at the relevant velocity range, $0.1 < \gamma\beta < 3$. The accuracy of the approximate description of the dynamics is important due to the strong dependence of the flux on the velocity of the emitting plasma (approx. $\propto (\gamma\beta)^4$, see be-

low). In addition, we provide an approximate analytic description for both the phase of rising flux, which was addressed in earlier papers (Nakar & Piran 2011; Kathirgamaraju et al. 2019), and for the phase of flux decline, which was not addressed in detail before.

The paper is organized as follows. The analytic expressions providing an approximate description of the non-thermal flux are derived in § 2. Their accuracy is estimated by a comparison to the results of numeric relativistic-hydrodynamic calculations in § 3. Our results are compared to those of earlier work in § 4. The implications of our results for future observations of the electromagnetic counterpart of GW170817 are discussed in § 5, and our conclusions are summarized in § 6.

2 ANALYTIC MODEL

As the ejecta expands, a forward shock is driven into the ISM and a reverse shock is driven into the ejecta (see Fig. 1). The kinetic energy of the ejecta decreases due to its deceleration by the reverse shock, and the energy is transferred to the shocked ISM plasma. The shocked ISM mass increases with the expanding shock radius, while its energy density decreases due to shock deceleration. The increase of the mass of hot plasma acts to increase the non-thermal emission, while the deceleration acts to suppress it (due both to the decreasing energy density and to the decreasing effect of flux enhancement due to relativistic expansion). For sufficiently steep drop of mass with velocity, $s_{\geq 5}$ as shown below, the former effect dominates and the non-thermal flux increases with time. This is due to the fact that the deceleration is slower for a steeper mass distribution, since the shocked ISM mass that needs to be accumulated in order to decelerate the shock below a certain velocity increases faster with decreasing velocity (as the ejecta mass increases faster with decreasing velocity).

For the steep mass profiles of the fast tail, inferred from numeric calculations, we thus expect the non-thermal flux to increase with time as long as the reverse shock propagates through the fast tail of the ejecta. Once the reverse shock penetrates into the bulk of the ejecta, where the mass distribution as function of velocity is shallow, the deceleration becomes more rapid and the flux begins to decrease. At late time, after the reverse shock crosses the entire ejecta and the expansion velocity becomes sub-relativistic, the flow approaches the non-relativistic Sedov-von Neumann-Taylor self-similar flow (Sedov 1946; Taylor 1950).

This section is organized as follows. The phase of rising flux, $t < t_{\text{peak}}$, is discussed in § 2.1, the asymptotic Sedov-von Neumann-Taylor phase, $t > t_{\text{ST}}$ is discussed in § 2.2, and the intermediate phase between them is discussed in § 2.3. A summary of the analytic results is given in § 2.4.

The hydrodynamic profiles are determined by three dimensional parameters, $\{M_0, n, c\}$ (the mass of the fast tail, the ISM density and the speed of light, respectively), and three dimensionless parameters, $\{\beta_0, s_{\text{ft}}, s_{\text{KN}}\}$. The dependence of the profiles on the dimensional parameters follows directly from dimensional considerations. The flow depends non-trivially only on the dimensionless parameters. The approximations that we provide are valid over a wide range of values of these parameters, $5 < s_{\text{ft}} < 12$, $1 < s_{\text{KN}} < 3$, $0.3 < \beta_0 < 0.9$.

2.1 Rising phase

In § 2.1.1 we first derive an approximate description of the dependence of the velocity of the shocked plasma, β_{SP} , and of the velocity $\beta_{\text{ej,RS}}$ of the un-shocked plasma at the position reached by the reverse shock, on radius R . We then derive an approximate expression for

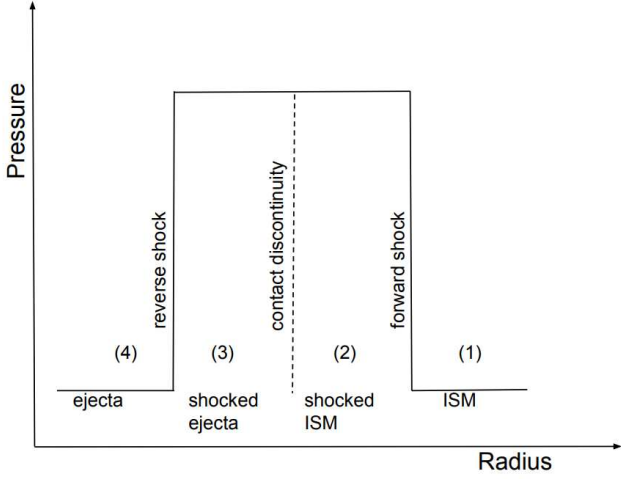


Figure 1. A schematic illustration showing the four regions of the forward-reverse shock structure described in § 2.1: (1) un-shocked ISM, (2) shocked ISM, (3) shocked ejecta, (4) un-shocked ejecta. The pressure in the un-shocked regions is negligible compared to that in the shocked regions, $p_1, p_4 \ll p_2, p_3$. The pressure and velocity are approximated in our analytic calculations as uniform within the shocked region, and the density is approximated as uniform within the two regions separated by the contact discontinuity.

t_{peak} , the (observed) time at which the flux peaks. In § 2.1.2 we use these results to derive an approximate description of the non-thermal flux.

2.1.1 Dynamics

Let us first obtain a qualitative estimate of the relation between the accumulated shocked ISM mass and the shocked ejecta mass. Consider ejecta of mass M_{ej} with uniform initial velocity, β_{ej} . A significant deceleration of the shell occurs when a significant fraction of its energy is transferred to the ISM. Assuming that the velocity of the shocked plasma is not far below the initial shell velocity, i.e. that the deceleration by the reverse shock is modest as justified below, this implies significant deceleration when the shocked ISM mass, M_{ISM} , reaches $M_{\text{ISM}} \approx M_{\text{ej}}/\gamma_{\text{ej}}$. This is due to the fact that the shell's initial energy is $0.5\beta_{\text{ej}}^2 M_{\text{ej}}c^2$ for $\beta_{\text{ej}} \ll 1$ and $\gamma_{\text{ej}}M_{\text{ej}}c^2$ for $\gamma_{\text{ej}} \gg 1$, while the shocked ISM energy is $\approx \beta_{\text{ej}}^2 M_{\text{ISM}}c^2$ and $\approx \gamma_{\text{ej}}^2 M_{\text{ISM}}c^2$ respectively. This result suggests that the position of the reverse shock within the ejecta, i.e. the initial velocity $\beta_{\text{ej,RS}}$ of the ejecta shell that is reached by the reverse shock, is (implicitly) determined by $M(> \gamma_{\text{ej,RS}}\beta_{\text{ej,RS}}) = \gamma_{\text{ej,RS}}(R)M_{\text{ISM}}(R)$, where $\gamma(R)$ is the Lorentz factor corresponding to $\beta(R)$.

A more accurate approximation, in particular taking into account the deceleration due to the reverse shock, is obtained as follows. We assume that at any given R the velocity and pressure profiles within the shocked ejecta/ISM plasmas (see fig. 1) are uniform, and that the shocked ejecta/ISM densities are uniform within the regions separated by the contact discontinuity. Denoting the mass of the ejecta shocked by the reverse shock as $M_{\text{ej,RS}}(R)$, we obtain (using Eq. (1)) the un-shocked ejecta number density and velocity ahead of the reverse shock, $n_{\text{ej,RS}}(R, M_{\text{ej,RS}}(R))$ and $\beta_{\text{ej,RS}}(R, M_{\text{ej,RS}}(R))$. Given $n_{\text{ej,RS}}(R, M_{\text{ej,RS}}(R))$ and the number density of the ISM, n , a relation between $\beta_{\text{ej,RS}}$ and the velocity of the shocked plasma, β_{SP} , is obtained by requiring the pressures behind the forward and reverse

shocks to be equal, thus determining $\beta_{\text{SP}}(R, M_{\text{ej,RS}}(R))$. Finally, $M_{\text{ej,RS}}(R)$ is determined by requiring the energy in the shocked ejecta and ISM plasma to equal the initial kinetic energy carried by the ejecta mass $M_{\text{ej,RS}}(R)$ (the thicknesses of the two shocked plasma regions, which are required for determining the internal energy of the shocked plasma, are determined by conservation of mass).

The solution for $\beta_{\text{SP}}(R)$ is obtained by numerically solving the pressure equilibrium and energy conservation equations described in the preceding paragraph. We use an EoS of the form $p = (\hat{\gamma} - 1)e$ with adiabatic index $\hat{\gamma}(e/n)$ varying from $4/3$ to $5/3$ following the analysis of Sygne (1957) for a plasma of protons and electrons. This is not accurate for the shocked ejecta plasma, which is composed of a wide range of nuclei. However, the dependence of the results on the exact form of $\hat{\gamma}(e/n)$ for the shocked ejecta plasma is weak (as verified by the numeric calculations). Once the hydrodynamic evolution is determined, we calculate the non-thermal flux as described in the following subsection.

For the purpose of deriving analytic expressions for the flux, it is useful to derive analytic approximations for the dynamics. We give below several useful approximations, which we found to provide a good description of the dynamics obtained by solving the equations described above for a wide range of ejecta parameters, $5 < s_{\text{fit}} < 12$, $0.2 < \gamma_{\text{ej,RS}}\beta_{\text{ej,RS}} < 6$. We find that $\beta_{\text{ej,RS}}(R)$ is well approximated by the implicit relation

$$M(> \gamma_{\text{ej,RS}}(R)\beta_{\text{ej,RS}}(R)) = \gamma_{\text{ej,RS}}(R)M_{\text{ISM}}(R), \quad (3)$$

that the ratio of the pre- and post-shock velocities is approximately given by

$$\frac{\gamma_{\text{ej,RS}}(R)\beta_{\text{ej,RS}}(R)}{\gamma_{\text{SP}}(R)\beta_{\text{SP}}(R)} = 1.7, \quad (4)$$

and that $R \approx \beta_{\text{ej,RS}}ct_s$, where t_s is the time measured at the rest frame of the source ejecting the expanding plasma.

Let us consider next the radius and velocity of the shocked plasma dominating the emission that contributes to the flux observed by a distant observer at that time t . Photons emitted from the shock front along a line making an angle θ with respect to the line of sight are observed at time t related to R by $R = \beta_{\text{ej,RS}}ct/(1 - \beta_{\text{ej,RS}}\cos\theta)$ (where we have used $R \approx \beta_{\text{ej,RS}}ct_s$ and $t_s = t/(1 - \beta_{\text{ej,RS}}\cos\theta)$). The emission from a ring of opening angle θ and thickness $d\theta$ increases with θ due to the increase in ring area, and decreases with θ due to the decrease in the Lorentz boost, $1/(\gamma^2(1 - \beta\cos\theta)^2)$. We therefore estimate the angle dominating the flux observed at time t as the angle for which $\partial_{\theta}(2\pi\sin\theta/(\gamma^2(1 - \beta\cos\theta)^2)) = 0$,

$$\cos\theta = -\frac{1}{2\beta} + \sqrt{2 + \frac{1}{4\beta^2}}. \quad (5)$$

We therefore approximate

$$R = \frac{\beta_{\text{ej,RS}}ct}{\left(1.5 - \sqrt{2\beta_{\text{ej,RS}}^2 + 0.25}\right)}. \quad (6)$$

Adopting this approximation we have

$$\begin{aligned} \gamma_{\text{ej,RS}}M_{\text{ISM}}(t) &= \frac{4\pi}{3}nm_p c^3 \frac{\gamma_{\text{ej,RS}}\beta_{\text{ej,RS}}^3}{\left(1.5 - \sqrt{2\beta_{\text{ej,RS}}^2 + 0.25}\right)^3} t^3 \\ &\approx \frac{4\pi}{3}nm_p c^3 12(\gamma_{\text{ej,RS}}\beta_{\text{ej,RS}})^{5.5} t^3, \end{aligned} \quad (7)$$

where the last approximation holds (to $\sim 10\%$) for $0.3 < \gamma\beta < 2.5$.

Using Eq. (3) we finally obtain

$$\gamma_{\text{ej,RS}}\beta_{\text{ej,RS}} = \left(\frac{t}{t_R}\right)^{-\frac{3}{5.5+s_{\text{ft}}}}, \quad t_R \equiv \left(\frac{M_0(\gamma_0\beta_0)^{s_{\text{ft}}}}{16\pi n m_p c^3}\right)^{\frac{1}{3}}. \quad (8)$$

Eqs. (4) and (8) determine the velocity of the shocked plasma dominating the emission of flux measured by a distant observer at time t .

Using the above approximations, we find that the observed time at which the flux peaks, i.e. the observed time at which the reverse shock reaches the shallow $\gamma\beta < \gamma_0\beta_0$ part of the ejecta, is given by

$$t_{\text{peak}} \approx \left(\frac{3M_0}{4\pi n m_p \gamma_0}\right)^{\frac{1}{3}} \left(\frac{1.5 - \sqrt{0.25 + 2\beta_0^2}}{c\beta_0}\right). \quad (9)$$

2.1.2 Non-thermal flux

The solution obtained for $\beta_{\text{SP}}(R)$ (and $\beta_{\text{FS}}(R)$, $\beta_{\text{ej,RS}}(R)$) by numerically solving the pressure equilibrium and energy conservation equations described in the preceding subsection, provide, under the approximation of uniform pressure, velocity, and density within the shocked plasma region, a full approximate description of the hydrodynamics- $p(r, t)$, $v(r, t)$, and $n(r, t)$. We use the hydrodynamic profiles to calculate the specific emissivity at the plasma frame, $j'_\nu(r, t)$ (following Rybicki & Lightman 1979), using the phenomenological description adopted for the magnetic field and for the electron energy distribution- assuming that the magnetic field and electrons carry fractions ε_B and ε_e of the internal energy density respectively, and that the electrons follow a power-law energy distribution. Using j'_ν , the specific intensity $I_\nu(\hat{\Omega})$ and the specific flux, F_ν , are derived numerically (properly accounting for relativistic and arrival time effects).

We derive below analytic expressions for F_ν , which provide a good (to 10's of percent) approximation for F_ν obtained numerically as described above for a wide range of parameters, $5 < s_{\text{ft}} < 12$, $0.2 < \gamma_{\text{ej,RS}}\beta_{\text{ej,RS}} < 6$. We consider in this derivation only the emission from the shocked ISM, that dominates over the emission from the shocked ejecta (as verified by the numeric calculations). The derivation given below provides the dependence on model parameters. Order unity corrections are applied to the numeric coefficients obtained in the derivation, in order to improve the agreement with the numeric results. We do not show in this section comparisons of the approximations to the numeric results. Instead, we show in § 3 direct comparison to the full numeric calculation, which includes a full numeric solution of the hydrodynamics equations (instead of the approximate treatment used in this subsection).

We first consider the flux produced by a spherical shock driven by a piston of fixed Lorentz factor γ , and then derive the flux obtained for the ejecta under consideration by using the approximate analytic dependence of $\gamma(t)$ derived in the preceding subsection. Approximating the internal energy carried by the shocked plasma as $E(R) = \gamma(\gamma - 1)M(R)c^2$, the luminosity observed by a distant observer, for the case where electrons lose all their energy via synchrotron emission on a time scale short compared to the expansion time, is $L = \varepsilon_e dE/dt$. We denote by γ_c the (plasma frame) electron Lorentz factor above which the electron energy loss time is short (compared to the expansion time), and by ν_c the corresponding (observer frame) synchrotron frequency. Noting that for a power-law energy distribution of electrons the specific flux at $\nu > \nu_c$ follows

$F_\nu \propto \nu^{-p/2}$, we have for $\nu > \nu_c$

$$L_\nu = 2\pi\gamma(\gamma - 1)\frac{R^3}{t}\varepsilon_e n m_p c^2 l_p \frac{\nu^{-p/2}}{\nu_m^{1-p/2}}, \quad (10)$$

where

$$l_p = \frac{p-2}{1 - (\gamma_{\text{max}}/\gamma_{\text{min}})^{2-p}}, \quad l_p \xrightarrow{p \rightarrow 2} \frac{1}{\ln(\gamma_{\text{max}}/\gamma_{\text{min}})}, \quad (11)$$

and ν_m is the characteristic observed frequency of the synchrotron emission of the lowest energy electrons, with $\gamma_e = \gamma_{\text{min}}$. Based on particle acceleration calculations as well as observations, we expect electrons to be accelerated over many decades in energy, $\gamma_{\text{max}}/\gamma_{\text{min}} \gg 1$. The dependence on $\gamma_{\text{max}}/\gamma_{\text{min}}$ is thus weak. When presenting numeric results below, we use $\gamma_{\text{max}}/\gamma_{\text{min}} = 10^5$ (Sironi et al. 2013).

For $\nu < \nu_c$, the specific luminosity is suppressed by a factor $(\nu/\nu_c)^{1/2}$. The self-absorption frequency, ν_a , is expected to be low, and we therefore consider the emission only at $\nu > \nu_a$.

Let us estimate next the frequencies ν_m and ν_c . The characteristic plasma frame frequency of the synchrotron emission of electrons with Lorentz factor γ_e and isotropic velocity distribution is $\gamma_e^2 \sqrt{(\pi u_B/2)} e / (m_e c)$, where u_B is the (plasma frame) magnetic field energy density. Approximating the post shock energy density, $2nm_p v^2$ for non-relativistic and $4\gamma^2 nm_p c^2$ for highly relativistic shocks, by $4\gamma(\gamma - 1)nm_p c^2$, we have $u_B = 4\varepsilon_B \gamma(\gamma - 1)nm_p c^2$. Defining

$$\nu_s = \frac{e}{m_e} \sqrt{2\pi\varepsilon_B nm_p}, \quad (12)$$

the observer frame synchrotron frequencies are thus

$$\nu_m = \frac{\gamma_{\text{min}}^2 \gamma^{-\frac{1}{2}} (\gamma - 1)^{\frac{1}{2}} \nu_s}{(1.5 - \sqrt{2\beta^2 + 0.25})}, \quad \nu_c = \frac{\gamma_c^2 \gamma^{-\frac{1}{2}} (\gamma - 1)^{\frac{1}{2}} \nu_s}{(1.5 - \sqrt{2\beta^2 + 0.25})}. \quad (13)$$

γ_{min} is obtained by requiring the average energy per electron to equal a fraction ε_e of the post-shock internal energy per particle, $(\gamma - 1)m_p c^2$, while γ_c is obtained by requiring the (plasma frame) synchrotron loss time, $m_e c^2 / (\gamma_e (4/3)\sigma_T c u_B)$, to be equal to the time measured at the plasma frame, $t/\gamma / (1.5 - \sqrt{2\beta^2 + 0.25})$. This yields

$$\gamma_{\text{min}} = \frac{l_p(\gamma - 1)\varepsilon_e m_p}{p - 1} \frac{1}{m_e}, \quad (14)$$

$$\gamma_c = \frac{(1.5 - \sqrt{2\beta^2 + 0.25})m_e}{4(\gamma - 1)\varepsilon_B \left(\frac{4}{3}\right)\sigma_T n m_p c t}.$$

Eqs. (10-14) provide an approximate description of $L_\nu(t)$ for time independent γ . In order to obtain an approximate analytic description of L_ν for the shock driven by the ejecta described by Eq. (1), we replace the time independent β and $R(t)$ in these equations with $\beta_{\text{SP}}(t)$ and $R(t)$ obtained in the preceding sub-section, using the appropriate time derivative dE/dt . We approximate the resulting functional dependence on γ and β by power-laws of the form $\propto (\gamma\beta)^\lambda$. This enables us to use Eqs. (4) and (8) to derive analytic expressions for ν_c , ν_m and L_ν . For ν_m , for example, we have

$$\nu_m = \left(\frac{l_p(\gamma - 1)\varepsilon_e m_p}{p - 1} \frac{1}{m_e}\right)^2 \frac{\gamma^{-1/2}(\gamma - 1)^{\frac{1}{2}} \nu_s}{(1.5 - \sqrt{2\beta^2 + 0.25})}$$

$$\approx \left(\frac{l_p \varepsilon_e m_p}{(p - 1)m_e}\right)^2 0.2(\gamma_{\text{SP}}\beta_{\text{SP}})^{5.1} \nu_s, \quad (15)$$

where the approximation holds (to 10%) for $0.3 < \gamma_{\text{SP}}\beta_{\text{SP}} < 2.5$. Using this approximation with Eqs. (4) and (8) yields an analytic expression for $v_m(t)$. The $(\gamma\beta)^\lambda$ power-law approximations used for v_c and L_ν are given in App. A, and the resulting analytic expressions are given in § 2.4.

2.2 Sedov–von Neumann–Taylor (SvNT) phase

At late time, after the reverse shock crosses the entire ejecta and once the ejecta decelerates to sub-relativistic, $\beta_s \lesssim 0.05$, velocity, the flow approaches the self-similar behavior described by the SvNT solution for an explosion with energy given by the initial kinetic energy, E , of the ejecta. At this stage, the shock radius is given by $R_{\text{ST}}(t) = \zeta \left(\frac{E}{\rho}\right)^{\frac{1}{5}} t^{\frac{2}{5}}$, where ζ is an order unity dimensionless parameter depending on the adiabatic index $\hat{\gamma}$ of the shocked material, $\zeta = 1.15$ for $\hat{\gamma} = \frac{5}{3}$. We therefore estimate the time beyond which the flow is well approximated by the SvNT solution as

$$t_{\text{ST}} \approx \left(0.05 \frac{2.5c}{\zeta} \left(\frac{E}{\rho}\right)^{-\frac{1}{5}}\right)^{-\frac{5}{2}}, \quad (16)$$

The synchrotron luminosity produced by the collisionless shock is derived in a manner similar to that of the preceding sub-section. Assuming that a fraction ε_e of the internal energy flux through the shock, $4\pi \frac{4\hat{\gamma}}{(\hat{\gamma}+1)^2} \frac{1}{2} \rho v_s^3 R^2$, is carried by electrons, the luminosity at frequencies $\nu > \nu_c$ (where electrons lose all their energy over a time short compared to the expansion time), is given by

$$L_{\nu, \text{ST}} = \frac{4\pi\hat{\gamma}}{(\hat{\gamma}+1)^2} \varepsilon_e \rho v_s^3 R^2 l_p \frac{v^{-\frac{p}{2}}}{\left(\beta_{\text{min}}^2 v_{m, \text{ST}}\right)^{1-\frac{p}{2}}}, \quad (17)$$

where

$$\beta_{\text{min}} = \frac{l_p}{p-1} \varepsilon_e \frac{m_p}{m_e} \frac{9\beta_s^2}{32} \quad (18)$$

is the velocity (at the plasma frame) of the lowest energy electrons. Note that the lowest energy electrons are not relativistic for $\beta_s \ll 1$, and we have therefore used in this calculation an electron energy distribution that follows a power-law in momentum, $dn_e/d(\gamma\beta)_e \propto (\gamma\beta)_e^{-p}$ (Krymskii 1977; Blandford & Ostriker 1978; Bell 1978). The corresponding observer frame minimum and cooling frequencies are

$$v_{m, \text{ST}} = \frac{3\beta_s}{4\sqrt{2}} v_s, \quad v_{c, \text{ST}} = \gamma_{c, \text{ST}}^2 \frac{3\beta_s}{4\sqrt{2}} v_s, \quad (19)$$

where

$$\gamma_{c, \text{ST}} = \frac{8m_e}{9\beta_s^2 \varepsilon_B \left(\frac{4}{3}\right) \sigma_T \rho c t}. \quad (20)$$

The specific flux obtained using Eqs. (17)-(20) is given below by Eqs. (32-33). The analytic description provides a good approximation (within 10's of percent) to the results obtained by numerically calculating the synchrotron flux using the analytic self-similar SvNT hydrodynamic profiles (calculating j_ν , I_ν and F_ν adopting the phenomenological assumptions described above regarding the magnetic field energy density and the electron energy distribution). This is demonstrated in figure 2, showing a comparison of the analytic and numeric results for $v_{m, \text{ST}}, v_{a, \text{ST}} < \nu < v_{c, \text{ST}}$.

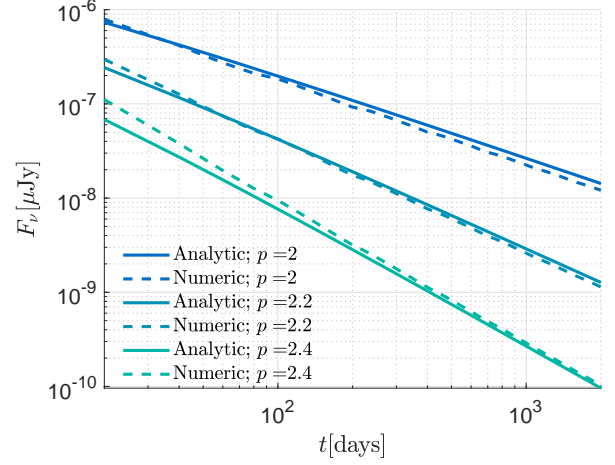


Figure 2. A comparison of the analytic (solid lines, Eqs. (32-33)) and numeric (dashed lines) calculations of the synchrotron flux during the phase of non-relativistic self-similar expansion (where the flow is described by the SvNT solutions). The parameter values chosen for the calculations are $E = 10^{42}$ erg, $\varepsilon_e = 10^{-1}$, $\varepsilon_B = 10^{-2}$ and $n = 10^{-2}$ cm $^{-3}$. Results are shown for $v_{m, \text{ST}}, v_{a, \text{ST}} < \nu < v_{c, \text{ST}}$ and observer distance of $D = 10$ Mpc.

2.3 Intermediate phase

We consider here the phase during which the reverse shock propagates through the shallower, $\beta < \beta_0$, part of the ejecta. Using the semi-analytic calculation of the dynamics described in § 2.1.1, we find that $\gamma_{\text{ej,RS}}\beta_{\text{ej,RS}}$ is well described for $1 < s_{\text{KN}} < 3$ and $0.1 < \gamma_{\text{ej,RS}}\beta_{\text{ej,RS}} < 0.7$ by

$$\gamma_{\text{ej,RS}}\beta_{\text{ej,RS}} \propto t^{-3/(4.7+s_{\text{KN}})}. \quad (21)$$

The synchrotron flux is then derived in a manner similar to that of § 2.1.2. The $(\gamma\beta)^\lambda$ power-law approximations used for v_c and L_ν in this regime are given in App. A, and the resulting analytic expressions are given in § 2.4.

2.4 Summary of the analytic model results

We summarize below the analytic results derived in the preceding sub-sections for the specific flux at the three time regimes, $t < t_{\text{peak}}$, $t > t_{\text{ST}}$ and $t_{\text{peak}} < t < t_{\text{ST}}$, and provide at the end an interpolation formula that provides a good approximation for the specific flux at all times. The numerical values of the parameters are normalized to those expected to be relevant for NS merger ejecta.

Analytic expressions for the synchrotron emission produced by an ejecta with a power-law dependence of ejecta energy on momentum, Eq. (2), may be obtained from the results given in this sub-section by the substitutions

$$M_0 = 1.5 \frac{E_0}{(\gamma_0\beta_0)^2 c^2}, \quad (22)$$

$$s_{\text{ft}} = \alpha_{\text{ft}} + 2, \quad s_{\text{KN}} = \alpha_{\text{KN}} + 1.5.$$

The three characteristic time scales are given by Eqs. (8), (9)

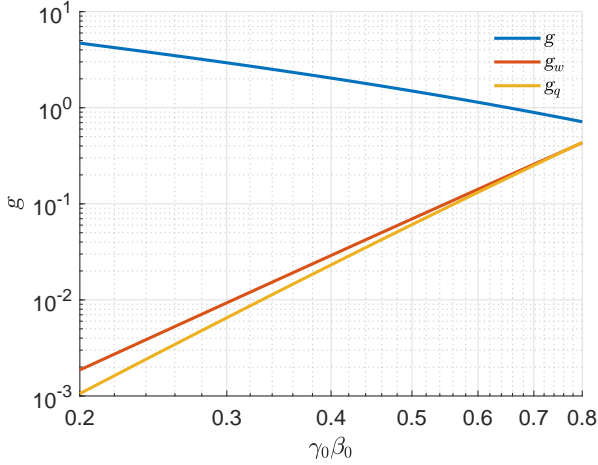


Figure 3. The functions $g(\beta_0)$ and $g_{w,q}(\beta_0, p, s)$ (Eqs. (23) and (31)) for $s = 7$, $p = 2.2$.

and (16)

$$t_R = 51 \left(\frac{M_{R,-6}}{n-2} \right)^{\frac{1}{3}} \text{ days},$$

$$t_{\text{peak}} = 550g(\beta_0) \left(\frac{M_{0,-4}}{n-2} \right)^{\frac{1}{3}} \text{ days}, \quad g(\beta_0) = \frac{1.5 - \sqrt{0.25 + 2\beta_0^2}}{\gamma_0^{\frac{1}{3}} \beta_0},$$

$$t_{\text{ST}} = 2.9 \times 10^4 \left(\frac{E_{50}}{n-2} \right)^{\frac{1}{3}} \text{ days}, \quad (23)$$

where

$$M_R \equiv M(\gamma\beta > 1) = M_0(\gamma_0\beta_0)^{s_{\text{ft}}}, \quad (24)$$

and we use $n = 10^{-2}n_{-2}\text{cm}^{-3}$, $E = 10^{50}E_{50}\text{erg}$ (where E is the total kinetic energy of the ejecta, $E(\gamma\beta > 0.1)$), $M_R = 10^{-6}M_{R,-6}M_{\odot}$ and $M_0 = 10^{-4}M_{0,-4}M_{\odot}$. The function $g(\beta_0)$ is plotted in Fig. 3. For an ejecta with a power-law dependence of ejecta energy on momentum, Eq. (2),

$$E_R \equiv E(\gamma\beta > 1) = E_0(\gamma_0\beta_0)^{\alpha} = \frac{M_R c^2}{1.5}. \quad (25)$$

The specific flux at $t < t_{\text{peak}}$ is given by Eqs. (10-14)

$$F_{\nu,\text{ft}} = D_{26.5}^{-2} \varepsilon_{e,-1}^{p-1} f_{\text{ft}}(p) \times \begin{cases} 7.7 \varepsilon_{B,-2}^{\frac{p-2}{4}} n_{-2}^{\frac{3p-2}{4}} M_{R,-6}^{\frac{2}{3}} \nu_{9.5}^{-\frac{p}{2}} \left(\frac{t}{t_R} \right)^{w_{\text{ft}}} \text{ mJy} & \text{for } \nu > \nu_{c,\text{ft}}, \\ 0.1 \varepsilon_{B,-2}^{\frac{p+1}{4}} n_{-2}^{\frac{p+1}{4}} M_{R,-6} \nu_{9.5}^{\frac{1-p}{2}} \left(\frac{t}{t_R} \right)^{q_{\text{ft}}} \mu\text{Jy} & \text{for } \nu < \nu_{c,\text{ft}}, \end{cases} \quad (26)$$

with $D = 10^{26.5} D_{26.5}\text{cm}$, $\nu = 10^{9.5} \nu_{9.5}\text{Hz}$, $\varepsilon_e = 10^{-1} \varepsilon_{e,-1}$ and $\varepsilon_B = 10^{-2} \varepsilon_{B,-2}$,

$$w_{\text{ft}} = \frac{5 - 7.5p + 2s_{\text{ft}}}{5.5 + s_{\text{ft}}}, \quad q_{\text{ft}} = \frac{4.5 - 7.5p + 3s_{\text{ft}}}{5.5 + s_{\text{ft}}}, \quad (27)$$

and

$$f_{\text{ft}}(p) = 960 \times 8.8^{-p} (2.5 - 0.7p) (p-1)^{2-p} (l_p)^{p-1}. \quad (28)$$

$f_{\text{ft}}(p)$ deviates from unity by less than 30% for $2 < p < 2.5$ (the

origin of $8.8^{-p} (2.5 - 0.7p)$ factor is in the normalization chosen for the parameter values and the power-law approximation (App. A)).

The cooling frequency and $\gamma_{\text{SP}}\beta_{\text{SP}}(t)$ at $t < t_{\text{peak}}$ are given by Eqs. (4), (8) and (13)

$$\nu_{c,\text{ft}} = 1.9 \times 10^{10} \varepsilon_{B,-2}^{-\frac{3}{2}} n_{-2}^{-\frac{5}{6}} M_{R,-6}^{-\frac{2}{3}} \left(\frac{t}{t_R} \right)^{\frac{0.7-2s_{\text{ft}}}{5.5+s_{\text{ft}}}} \text{ GHz}, \quad (29)$$

$$\gamma_{\text{SP}}\beta_{\text{SP}} = 0.6 \left(\frac{t}{t_R} \right)^{-\frac{3}{5.5+s_{\text{ft}}}}.$$

Notice that in the limit $s_{\text{ft}} \rightarrow \infty$, in which the mass increases very rapidly as the velocity is reduced, we have $\gamma\beta \propto t^0$ and $L_{\nu} \propto t^{3(2)}$ below (above) $\nu_{c,\text{ft}}$, corresponding to no deceleration.

The peak flux, $F_{\nu,\text{ft}}(t_{\text{peak}})$, is given by

$$F_{\nu,\text{peak}} = D_{26.5}^{-2} \varepsilon_{e,-1}^{p-1} f_{\text{ft}}(p) \times \begin{cases} 170 \varepsilon_{B,-2}^{\frac{p-2}{4}} n_{-2}^{\frac{3p-2}{4}} M_{0,-4}^{\frac{2}{3}} \nu_{9.5}^{-\frac{p}{2}} g_w \text{ mJy} & \text{for } \nu > \nu_{c,\text{peak}}, \\ 10 \varepsilon_{B,-2}^{\frac{p+1}{4}} n_{-2}^{\frac{p+1}{4}} M_{0,-4} \nu_{9.5}^{\frac{1-p}{2}} g_q \mu\text{Jy} & \text{for } \nu < \nu_{c,\text{peak}}, \end{cases} \quad (30)$$

where $\nu_{c,\text{peak}} = \nu_{c,\text{ft}}(t_{\text{peak}})$ and

$$g_w = 2.3^{w_{\text{ft}}} (\gamma_0\beta_0)^{\frac{s_{\text{ft}}}{3}(2-w_{\text{ft}})} (g(\beta_0))^{w_{\text{ft}}} \approx 1.1(\gamma_0\beta_0)^{2.3p-1},$$

$$g_q = 2.3^{q_{\text{ft}}} (\gamma_0\beta_0)^{s_{\text{ft}}(1-\frac{q_{\text{ft}}}{3})} (g(\beta_0))^{q_{\text{ft}}} \approx 1.2(\gamma_0\beta_0)^{2.2p-0.5}. \quad (31)$$

The functions $g_{w,q}(\beta_0, p = 2.2, s_{\text{ft}} = 7)$ are plotted in Fig. 3.

The specific flux at $t > t_{\text{ST}}$ is given by Eqs. (16-20)

$$F_{\nu,\text{ST}} = D_{26.5}^{-2} \varepsilon_{e,-1}^{p-1} f_{\text{ST}}(p) \times \begin{cases} 1 \varepsilon_{B,-2}^{\frac{p-2}{4}} n_{-2}^{\frac{3p-2}{4}} E_{50}^{\frac{2}{3}} \nu_{9.5}^{-\frac{p}{2}} \left(\frac{t}{t_{\text{ST}}} \right)^{w_{\text{ST}}} \text{ mJy} & \text{for } \nu > \nu_{c,\text{ST}}, \\ 0.1 \varepsilon_{B,-2}^{\frac{p+1}{4}} n_{-2}^{\frac{p+1}{4}} E_{50} \nu_{9.5}^{\frac{1-p}{2}} \left(\frac{t}{t_{\text{ST}}} \right)^{q_{\text{ST}}} \mu\text{Jy} & \text{for } \nu < \nu_{c,\text{ST}}, \end{cases} \quad (32)$$

with

$$w_{\text{ST}} = \frac{20 - 15p}{10}, \quad q_{\text{ST}} = \frac{21 - 15p}{10}, \quad (33)$$

and

$$f_{\text{ST}}(p) = 1.4 \times 10^{10} \left(2 \times 10^4 \right)^{-p} (p-1)^{2-p} (l_p)^{p-1}. \quad (34)$$

$f_{\text{ST}}(p)$ is bounded by $0.75 < f_{\text{ST}}(p) < 3$ for $2 < p < 2.5$ (The origin of the $(2 \times 10^4)^{-p}$ factor is the normalization chosen for the values of the parameters).

The cooling frequency at $t > t_{\text{ST}}$ is given by Eqs. (19-20)

$$\nu_{c,\text{ST}} = 3.7 \times 10^8 \varepsilon_{B,-2}^{-\frac{3}{2}} E_{50}^{-\frac{2}{3}} n_{-2}^{-\frac{5}{6}} \left(\frac{t}{t_{\text{ST}}} \right)^{-\frac{1}{3}} \text{ GHz}. \quad (35)$$

For $t_{\text{peak}} < t < t_{\text{ST}}$ the specific flux is given by

$$F_{\nu,\text{KN}} = F_{\nu,\text{peak}} \times \begin{cases} \left(\frac{t}{t_{\text{peak}}} \right)^{w_{\text{KN}}} & \text{for } \nu > \nu_{c,\text{KN}}, \\ \left(\frac{t}{t_{\text{peak}}} \right)^{q_{\text{KN}}} & \text{for } \nu < \nu_{c,\text{KN}}, \end{cases} \quad (36)$$

with

$$w_{\text{KN}} = \frac{7.4 - 7.5p + 2s_{\text{KN}}}{4.7 + s_{\text{KN}}}, \quad q_{\text{KN}} = \frac{7.5 - 7.5p + 3s_{\text{KN}}}{4.7 + s_{\text{KN}}}. \quad (37)$$

The cooling frequency is given by

$$\nu_{c,\text{KN}} = \nu_{c,\text{ft}}(t_{\text{peak}}) \left(\frac{t}{t_{\text{peak}}} \right)^{\frac{0.5-2s_{\text{ft}}}{4.7+s_{\text{ft}}}}. \quad (38)$$

The $\nu < \nu_c$ specific flux is well described at all time by the interpolation

$$F_\nu = \left(0.5 F_{\nu, \text{peak}}^{-5} \left(\left(\frac{t}{t_{\text{peak}}} \right)^{-5q_{\text{ft}}} + \left(\frac{t}{t_{\text{peak}}} \right)^{-5q_{\text{KN}}} \right) + \left(F_{\nu, \text{ST}}(t_{\text{ST}}) \left(\frac{t}{t_{\text{ST}}} \right)^{q_{\text{ST}}} \right)^{-5} \right) \quad (39)$$

Here, $F_{\nu, \text{peak}}$ is given by Eq. (30), t_{peak} is given by Eq. (23), q_{ft} is given by Eq. (27), q_{KN} is given by Eq. (37) and $F_{\nu, \text{ST}}$ is given by Eq. (32). The specific flux at $\nu > \nu_c$ is well described by a similar expression, replacing q_X with w_X given by Eqs. (27), (37) and (33).

3 COMPARISON TO NUMERIC CALCULATIONS

We compare in this section the approximate analytic description of the non-thermal specific flux derived in the preceding section with the results obtained using full numeric solutions of the special relativistic 1D hydrodynamics equations (note that these are solutions of the exact hydrodynamic equations, rather than of the approximate equations derived in § 2.1.1). The numeric code we use is a 1D Lagrangian code using a predictor-corrector scheme, artificial viscosity, and time steps set by Courant–Friedrichs–Lewy (CFL) conditions. The code was verified by testing it against standard test problems (Sedov 1946; Martí & Müller 2003; Guzman et al. 2012). The EoS used in the numeric calculations is the same as that used for the approximate hydrodynamic solutions described in § 2.1.1, $p = (\hat{\gamma} - 1)e$ with adiabatic index $\hat{\gamma}(e/n)$ varying from 4/3 to 5/3 following the analysis of Sygne (1957). The initial conditions used for the numerical calculations were: density and velocity profiles given by Eq. (1) or (2) (the radius of a shell of mass $M (> \gamma\beta)$ is given by $r = \beta ct_0$ for some small chosen $t = t_0$), surrounded by a static uniform cold gas of number density n . The initial pressure is set to zero everywhere.

The emission of radiation was calculated, given a numeric solution for the flow fields, in a manner similar to that described at the opening of § 2.1.2. As explained at the opening of § 2, the dependence of the dynamics on the dimensional parameters $\{M_0, n, c\}$ follows directly from dimensional considerations, and the flow depends non-trivially only on the dimensionless parameters, $\{\beta_0, s_{\text{ft}}, s_{\text{KN}}\}$. We have explored a wide range of these parameters $5 < s_{\text{ft}} < 12$, $1 < s_{\text{KN}} < 3$, $0.3 < \beta_0 < 0.9$, and found 10's of percent agreement with our analytic approximation. We give below a few examples for the comparison of the full numeric calculation to the analytic approximation.

(i) In Fig. 4 we compare the numeric solution for the forward shock velocity and radius with the results of the semi-analytic solution for $t < t_{\text{peak}}$ described in § 2.1.1, and with the SvNT solution valid at late times. The good agreement supports the validity of both the numeric code and the semi-analytic solution of the dynamics.

(ii) In Fig. 5 we compare the specific flux obtained numerically with that given analytically in § 2.4, Eq. (39). The agreement is within 10's of percent for a wide range of relevant values of $\{\beta_0, s_{\text{ft}}, s_{\text{KN}}\}$.

(iii) In Fig. 6 we compare $F_{\nu, \text{peak}}$ obtained numerically with the analytic expression of Eq. (30) for a range of $\gamma_0\beta_0$ and s_{ft} values. The numeric and analytic results are within 10's of percent agreement.

(iv) In Fig. 7 we compare the numeric logarithmic slope of the temporal dependence of the specific flux at $t < t_{\text{peak}}$, $q_{\text{ft}} = d \log F_\nu(t) / d \log t$, with the analytic expression of Eq. (27) for a range of p and s_{ft} values, with a fixed β_0 . The numeric and analytic results are within 10's of percent agreement.

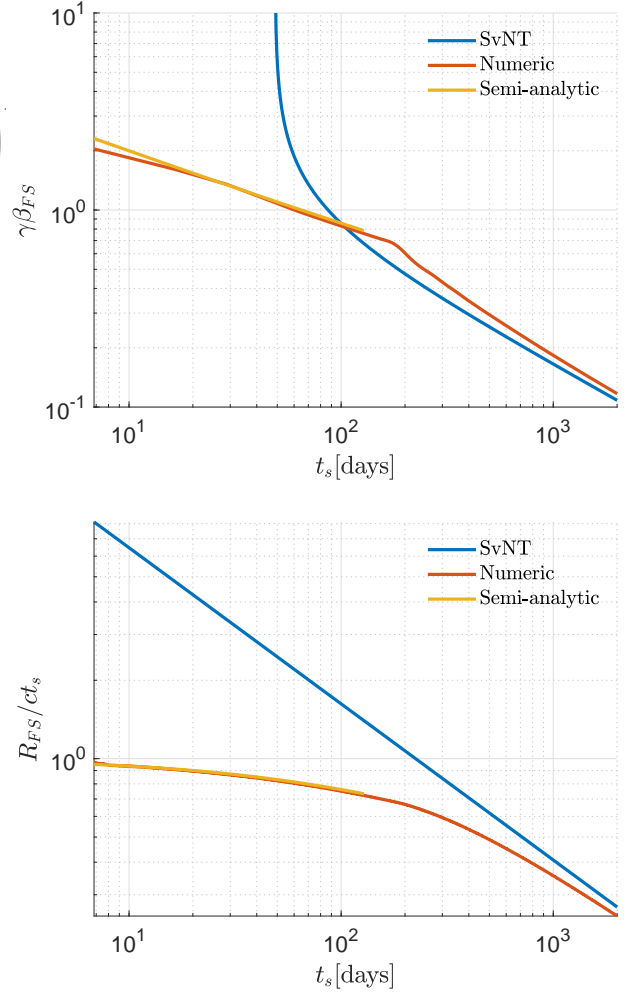


Figure 4. The forward shock $\gamma\beta$ (upper panel) and radius (lower panel) as a function of t_s , the time measured at the rest frame of the source ejecting the expanding plasma. The results of the numeric solution of the hydrodynamics (red) are compared with the semi-analytic solution described in § 2.1.1 (yellow), valid at early time (up to the time at which the reverse shock crosses the fast tail, $s_{\text{ft}} > 5$, ~ 150 days), and with the SvNT self-similar solution (red) valid at late times. The parameter values used for this calculation are $n = 3 \times 10^{-2} \text{cm}^{-3}$, $M_0 = 2 \times 10^{-6} M_\odot$, $s_{\text{ft}} = 7$, $s_{\text{KN}} = 1.5$ and $\gamma_0 = 1.35$.

(v) In Fig. 8 we compare t_{peak} obtained numerically with the analytic expression of Eq. (23) for a range of $\gamma_0\beta_0$ and s_{ft} values. The numeric and analytic results are within 10's of percent agreement.

A comparison of the analytic results with numeric results for a power-law dependence of ejecta energy on momentum, see Eq. (2), is given in § 4.

4 COMPARISON TO EARLIER WORK

We compare in this section our results with analytic results obtained in earlier papers. Nakar & Piran (2011) have considered a sub-relativistic shell of uniform β , and provided estimates of the peak time t_{peak} , which is valid for $\beta \ll 1$, and for the peak flux, which is based on extrapolation of expressions valid for highly relativistic ejecta. Kathirgamaraju et al. (2019) (hereafter KGB19) expanded the analysis of Nakar & Piran (2011), considering a shell with a single

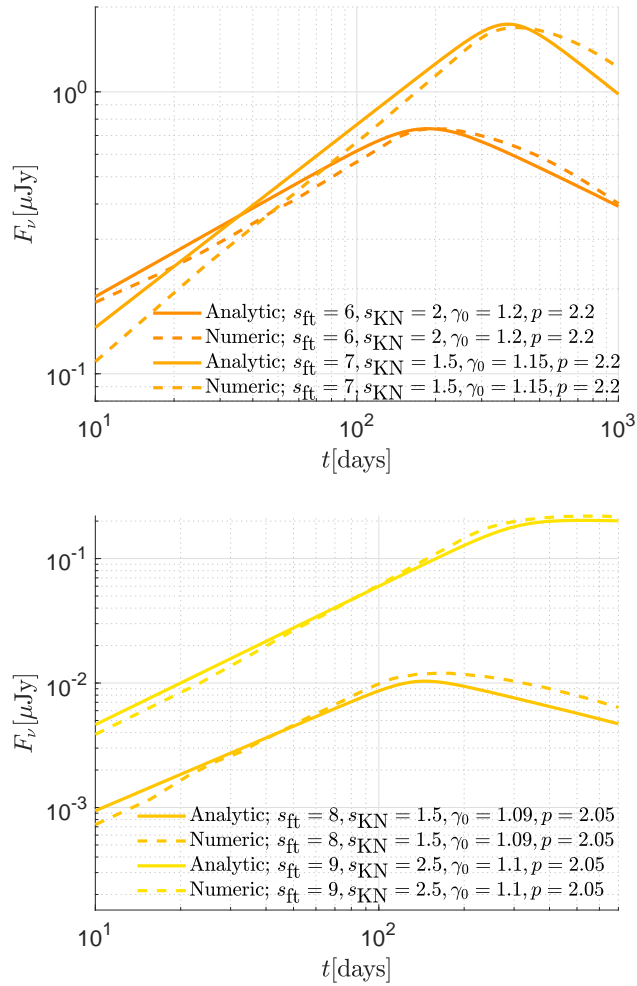


Figure 5. A comparison of the specific flux given analytically in § 2.4, Eq. (39) (solid lines) and the specific flux obtained numerically (dashed lines), for different values of the dimensionless parameters $\{s_{ft}, s_{KN}, \gamma_0, p\}$ and $\varepsilon_e = 10^{-1}$, $\varepsilon_B = 10^{-2}$, $M_0 = 1.2 \times 10^{-5} M_\odot / 5.2 \times 10^{-5} M_\odot / 7.6 \times 10^{-7} M_\odot / 1.1 \times 10^{-5} M_\odot$ (for $s_{ft} = 6/7/8/9$) and $n = 3 \times 10^{-2} \text{cm}^{-3}$. Results are shown for $v_m, v_a < v < 3\text{GHz} < v_c$ and observer distance of $D = 100\text{Mpc}$.

power-law energy distribution, $E(> \gamma\beta) = E_R(\gamma\beta)^{-\alpha}$ for $\beta > \beta_0$. They have used the peak flux derived in [Nakar & Piran \(2011\)](#), included an analysis of the dynamics to derive an expression for t_{peak} that takes into account relativistic effects and is valid for $\beta_0 < 0.5$, and used the results of [Barniol Duran et al. \(2015\)](#), that were derived for highly relativistic ejecta, for the power-law index q describing the $F_\nu \propto t^q$ time dependence of the specific flux at $t < t_{\text{peak}}$.

Let us first note that the results of [KGB19](#) are not self-consistent. At time $t < t_{\text{peak}}$, when the reverse shock propagates through the $\beta > \beta_0$ ejecta, the emission should depend on the shell energy, $E_0 = E(> \gamma_0\beta_0)$, and break/cutoff velocity, $\gamma_0\beta_0$, only through the combination $E_0(\gamma_0\beta_0)^\alpha = E_R$, since E_R completely determines the dynamics at this stage- the shock propagates through the $E(> \gamma\beta) = E_R(\gamma\beta)^{-\alpha} = E_0(\gamma_0\beta_0/\gamma\beta)^\alpha$ ejecta and the existence of a break/cutoff at $\gamma_0\beta_0$ does not affect the flow up to $t = t_{\text{peak}}$. See for example Eqs. (26) and (30)- the specific flux at $t < t_{\text{peak}}$ depends only on M_R , corresponding to E_R , while the peak flux depends on M_0 , corresponding to E_0 . The expression that [KGB19](#) provide for $F_\nu(t)$ depends on E_0 and $\gamma_0\beta_0$ separately, i.e. not only through the

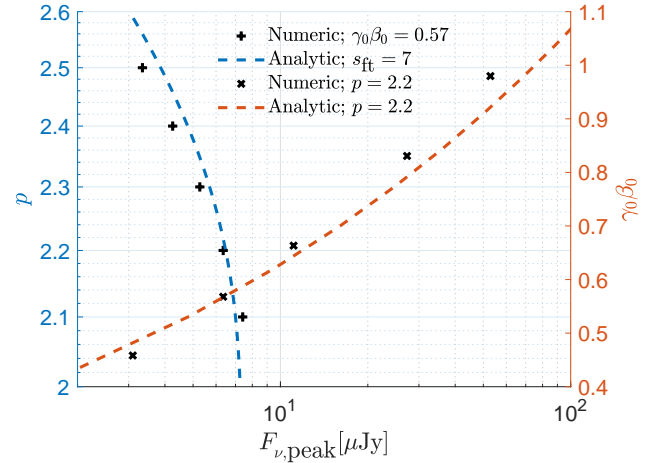


Figure 6. A comparison of the peak flux, $F_{\nu,\text{peak}}$, given by the analytic model, Eq. (30) (dashed lines), and that derived from numeric calculations ('+' and 'x' marks), as a function of p and of $\gamma_0\beta_0$, for $M_0 = 10^{-4} M_\odot$ and $n = 7 \times 10^{-2} \text{cm}^{-3}$. Results are shown for $v_m, v_a < v < 3\text{GHz} < v_c$ and observer distance of $D = 100\text{Mpc}$.

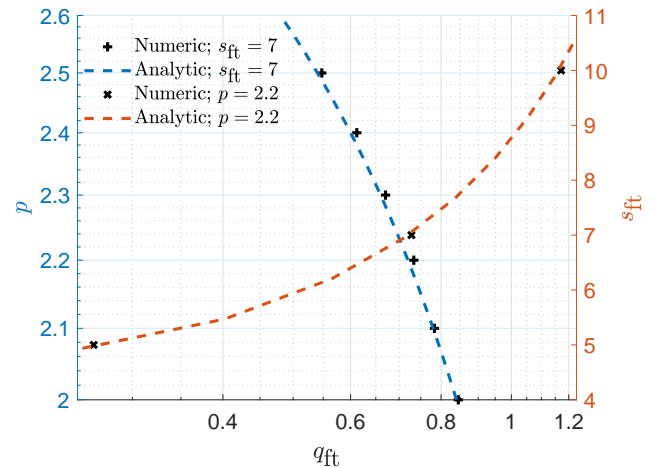


Figure 7. A comparison of the power-law index q_{ft} describing the $F_\nu \propto t^{q_{ft}}$ time dependence of the specific flux before the peak, given by the analytic model, Eq. (27) (dashed lines), and that derived from numeric calculations ('+' and 'x' marks), as a function of p and of s_{ft} , for $M_R = 10^{-6} M_\odot$, $n = 3 \times 10^{-3} \text{cm}^{-3}$ and $\gamma_0 = 1.35$.

combination $E_0(\gamma_0\beta_0)^\alpha = E_R$. This implies that it would predict different fluxes at $t < t_{\text{peak}}$ for ejecta with the same E_R , for which the predicted fluxes should be identical.

In Fig. 9 we compare the specific flux given by our analytic model, using Eq. (22), for an ejecta with a broken power-law dependence of ejecta energy on momentum, Eq. (2), with the specific flux obtained by our numeric calculations and that given by [KGB19](#). Our analytic expressions provide a good approximation (within 10's of percent) for the numerical results for different values of α_{ft} (5, 7) and β_0 (0.3, 0.65). The analytic expression of [KGB19](#), based on [Nakar & Piran \(2011\)](#), overestimates the specific flux by typically an order of magnitude, and significantly underestimate the peak time for $\beta = 0.65$. The ratio of the peak flux given by Eqs. (30-31) and (22)

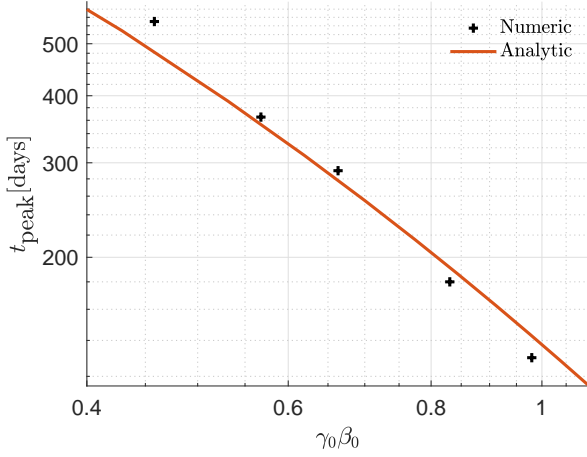


Figure 8. A comparison of the peak time, t_{peak} , given by the analytic model, Eq. (23) (solid line), and that obtained by numeric calculations (+ marks) for a range of $\gamma_0\beta_0$ values, for $M_0 = 10^{-4}M_\odot$ and $n = 7 \times 10^{-2}\text{cm}^{-3}$.

and that given by KGB19 is (pre-factor given for $p = 2.2$)

$$\frac{F_{\nu,\text{peak}}^{\text{KGB19}}}{F_{\nu,\text{peak}}} \approx 6\gamma_0^{2.5-2.2p} \beta_0^{0.3p-1}. \quad (40)$$

Fig. 10 shows the ratio between the logarithmic slope $q_{\text{ft}} = d \log F_\nu(t) / d \log t$ of the temporal dependence of the specific flux at $t < t_{\text{peak}}$ obtained by KGB19, $q_{\text{ft}}^{\text{KGB19}} = (3\alpha - 6(p-1))/(8 + \alpha_{\text{ft}})$, and our result, given by Eqs. (27) and (22), for different values of α_{ft} and p . Fig. 11 shows the ratio between the peak time, t_{peak} , obtained by KGB19, $t_{\text{peak}}^{\text{KGB19}} = 3.3 \left(\frac{E_{0.51}}{n-2}\right)^{\frac{1}{3}} \beta_0^{-\frac{2}{3}} \left(\frac{2+\alpha_{\text{ft}}}{\beta_0(5+\alpha_{\text{ft}})} - 1\right)$ years, and our result, given by Eqs. (23) and (22). As expected, the KGB19 expression provides a good approximation for t_{peak} for $\beta_0 < 0.5$.

5 GW170817 KN AFTERGLOW

The radio and X-ray observations of the electromagnetic counterpart of GW170817 are shown in figure 12. The measurements show a growing tension with the predictions of expanding jet models, but clear evidence for re-brightening associated with a fast tail is not (yet) present (Hajela et al. 2022; Nedora et al. 2021a; Balasubramanian et al. 2021, 2022; Troja et al. 2022; O'Connor & Troja 2022).

As noted in the introduction, the early evolution of the photospheric radius is consistent with a power-law mass distribution, $M(> \gamma\beta) \propto (\gamma\beta)^{-s_{\text{KN}}}$ with $s_{\text{KN}} \approx 1.6$ at $0.1 < \gamma\beta < 0.3$ and a total mass of $\approx 0.05M_\odot$ (Waxman et al. 2018). We consider the non-thermal emission that would be produced by a "fast-tail" extension of this power law to higher velocities, with s_{ft} in the range of 6-8 for $\beta > \beta_0 = 0.3$ ($M_0 = 8 \times 10^{-3}M_\odot$). Figure 12 shows the non-thermal specific flux predicted by our model for typical values expected for collisionless shocks, $\varepsilon_e = 10^{-1}$, $\varepsilon_B = 0.5 \times 10^{-2}$, $p = 2.15$, and conservatively low density, $n = 10^{-3}\text{cm}^{-3}$. The existence of a fast tail is expected to produce detectable radio and X-ray fluxes over a time scale of $\sim 10^4$ days.

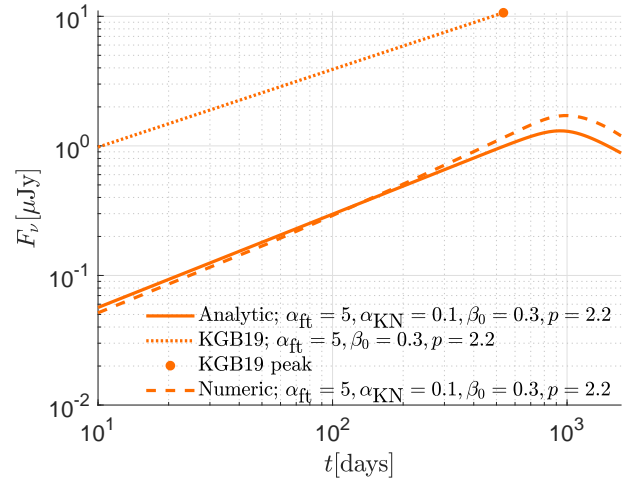
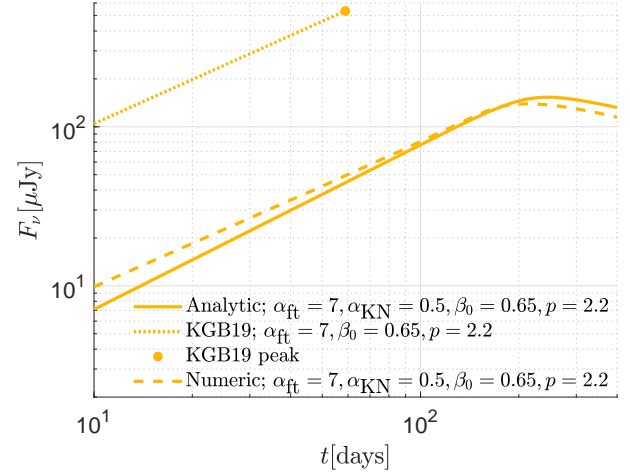


Figure 9. A comparison of the specific flux given analytically in § 2.4, Eqs. (22) and (39) (solid lines) with the specific flux obtained numerically (dashed lines) and that given analytically in KGB19, for ejecta profiles given by Eq. (2) with different values of the dimensionless parameters $\{\alpha_{\text{KN}}, \alpha_{\text{ft}}, \beta_0, p\}$ and $\varepsilon_e = 10^{-1}$, $\varepsilon_B = 10^{-2}$, $E_0 = 10^{50}\text{erg}/10^{49}\text{erg}$ (upper/lower panel) and $n = 3 \times 10^{-2}\text{cm}^{-3}$. Results are shown for $v_m/v_a < v < 3\text{GHz} < v_c$ and observer distance of $D = 100\text{Mpc}$.

6 SUMMARY

We have derived analytic expressions for the non-thermal synchrotron emission from spherical ejecta with broken power-law mass or energy distributions given by Eqs. (1) or (2). The analytic model equations are given in § 2.4. The analytic model results were compared in § 3 and in § 4 to the results of 1D numeric calculations for a wide range of ejecta parameter values characteristic of merger calculation results- a "shallow" mass (energy) distribution, $1 < s_{\text{KN}} < 3$, for the bulk of the mass (at $\gamma\beta \approx 0.2$), and a steep, $s_{\text{ft}} > 5$, "fast tail" mass (or energy) distribution. The analytic model provides an accurate (to 10's of percent) description of the evolution of the specific flux obtained in the numeric calculations, including at the phase of deceleration to sub-relativistic expansion- see figures 5-9. This is a significant improvement over earlier results, based on extrapolations of results valid for $\gamma\beta \gg 1$ and $\ll 1$ to $\gamma\beta \approx 1$, which overestimate the specific flux by an order of magnitude for typical parameter values and do not describe the emission beyond the time of peak flux (see discussion in § 4 and figures 9-11).

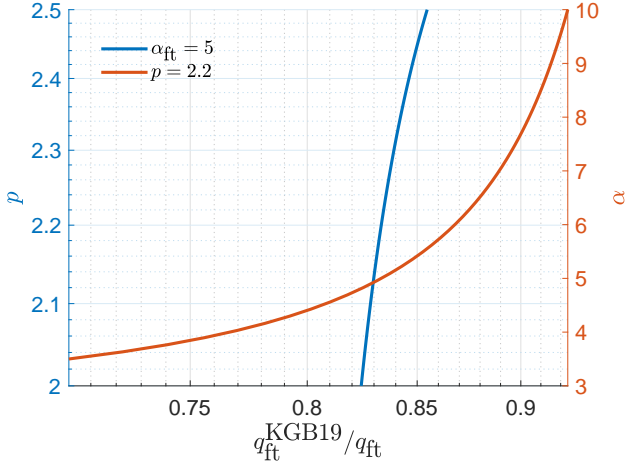


Figure 10. The ratio between the logarithmic slope $q_{\text{ft}} = d \log F_{\nu}(t) / d \log t$ of the temporal dependence of the specific flux at $t < t_{\text{peak}}$ obtained by KGB19 and our result, given by Eqs. (22) and (27), for different values of α_{ft} and p .

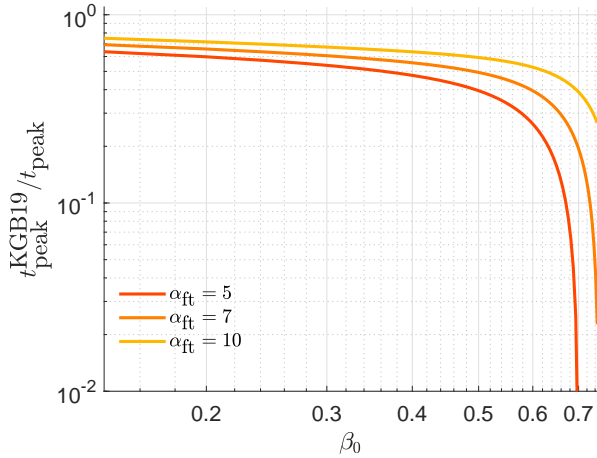


Figure 11. The ratio between the peak time, t_{peak} , obtained by KGB19, and our result, given by Eqs. (22) and (23).

The key results are the time and magnitude of the peak flux (at $\nu < \nu_c$), given by

$$t_{\text{peak}} = 550g(\beta_0) \left(\frac{M_{0,-4}}{n_{-2}} \right)^{\frac{1}{3}} \text{ days},$$

$$F_{\nu, \text{peak}} = 10D_{26.5}^{-2} \varepsilon_{e,-1}^{p-1} f_{\text{ft}}(p) \varepsilon_{B,-2}^{\frac{p+1}{4}} n_{-2}^{\frac{p+1}{4}} M_{0,-4} \nu_{9.5}^{\frac{1-p}{2}} g_q \mu\text{Jy}, \quad (41)$$

$$q_{\text{ft}} = \frac{4.5 - 7.5p + 3s_{\text{ft}}}{5.5 + s_{\text{ft}}}, \quad q_{\text{KN}} = \frac{7.5 - 7.5p + 3s_{\text{KN}}}{4.7 + s_{\text{KN}}},$$

where $q_{\text{ft}/\text{KN}}$ is the index describing the $F_{\nu} \propto t^{q_{\text{ft}/\text{KN}}}$ time dependence of the specific flux before/after the peak (for $6 < s_{\text{ft}} < 8$, $1 < s_{\text{KN}} < 2.5$ and $2 < p < 2.2$ we find $0.5 < q_{\text{ft}} < 1$ and

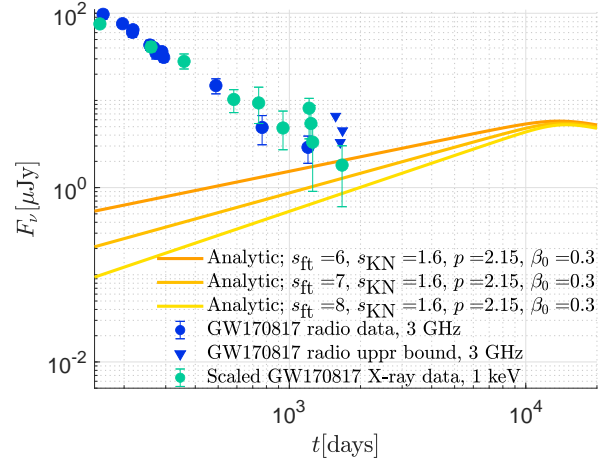


Figure 12. The radio and X-ray observations (symbols) of the electromagnetic counterpart of GW170817 (Troja et al. 2021, 2022; O'Connor & Troja 2022; Balasubramanian et al. 2021, 2022), and the radio flux (solid lines) predicted to be produced by a "fast-tail" extension, $M(> \gamma\beta) \propto (\gamma\beta)^{-s_{\text{ft}}}$ at $\beta > \beta_0 = 0.3$, of the mass distribution inferred from observations at lower velocity, $M(> \gamma\beta) \propto (\gamma\beta)^{-1.6}$ at $0.1 < \gamma\beta < 0.3$ and a total mass of $0.05M_{\odot}$ (Waxman et al. 2018). X-ray data are scaled by a factor 3×10^8 (corresponding to electron spectral index $p = 2.15$). Model results are shown for $\varepsilon_e = 10^{-1}$, $\varepsilon_B = 0.5 \times 10^{-2}$ and $n = 10^{-3} \text{cm}^{-3}$.

$-1 < q_{\text{KN}} < 0$), and

$$g(\beta_0) = \frac{1.5 - \sqrt{0.25 + 2\beta_0^2}}{\gamma_0^{\frac{1}{3}} \beta_0},$$

$$f_{\text{ft}}(p) = 960 \times 8.8^{-p} (2.5 - 0.7p)(p-1)^{-2-p} (l_p)^{p-1} \approx 1,$$

$$g_q = 2.3^{q_{\text{ft}}} (\gamma_0 \beta_0)^{s_{\text{ft}} \left(1 - \frac{q_{\text{ft}}}{3}\right)} (g(\beta_0))^{q_{\text{ft}}} \approx 1.2 (\gamma_0 \beta_0)^{2.2p-0.5}. \quad (42)$$

Here, $\gamma_0 \beta_0$ is the break between the fast part of the ejecta ($s_{\text{ft}} > 5$) and the slower part of the ejecta ($1 < s_{\text{KN}} < 3$), see Eq. (1), $M_0 = 10^{-4} M_{0,-4} M_{\odot}$ is the (total) mass of the fast tail, $n = 10^{-2} n_{-2} \text{cm}^{-3}$ is the ISM density, $\varepsilon_e = 10^{-1} \varepsilon_{e,-1}$ and $\varepsilon_B = 10^{-2} \varepsilon_{B,-2}$ are the fractions of internal energy carried by electrons and magnetic fields, and p is the electrons power-law index, $dn_e/d\gamma_e \propto \gamma_e^{-p}$. A routine calculating the specific flux based on the analytic results presented in this paper is available at https://gitlab.com/Gilad_Sadeh/sadeh-et-al-2022.

The flux peaks when the reverse shock crosses the steep fast tail, $\gamma\beta > \gamma_0 \beta_0$, part of the ejecta into the shallower part at lower velocity. It may be detected in the radio and X-ray bands, e.g. by the Very Large Array radio telescope (with a limiting sensitivity of $\sim 5 \mu\text{Jy}$ for 1–10GHz frequencies) and by the Chandra X-ray observatory (with a limiting sensitivity of $\sim 10^{-4} \mu\text{Jy}$ for 0.3–10keV photons for $\sim 10\text{ks}$ exposure time).

Our analytic model will enable a reliable direct inference of the values and uncertainties of model parameters from observations. While numeric calculations may provide higher accuracy predictions, the analytic model has a great advantage when inferring model parameters from observations, since it does not require detailed resource consuming calculations for each point in the model's multi-parameter space.

The late time non-thermal emission of GW170817 was considered in §5. Figure 12 shows the radio and X-ray flux that would

be produced by a fast tail, extending the observationally inferred $M(> \gamma\beta) \propto (\gamma\beta)^{-s_{\text{KN}}}$ with $s_{\text{KN}} \approx 1.6$ for $\beta < 0.3$ (Waxman et al. 2018), to higher velocity as $M(> \gamma\beta) \propto (\gamma\beta)^{-s_{\text{ft}}}$ with a range of s_{ft} values. Using typical values for $\varepsilon_{e,B}$ and p , and adopting a conservatively low density, $n = 10^{-3} \text{cm}^{-3}$, we find that the existence of a fast tail is expected to produce a detectable (few μJy) radio and ($10^{-15} \text{erg/cm}^2\text{s}$) X-ray fluxes over a time scale of $\sim 10^4$ days.

ACKNOWLEDGEMENTS

We thank Jonathan Morag and Arnab Sarkar for insightful discussions during the conduction of this work. Eli Waxman's research is partially supported by ISF, GIF and IMOS grants.

DATA AVAILABILITY

The data underlying this article will be shared following a reasonable request to the corresponding author. A routine calculating the specific flux based on the analytic results presented in this paper is available at https://gitlab.com/Gilad_Sadeh/sadeh-et-al-2022.

REFERENCES

- Arcavi I., et al., 2017, *Nature*, 551, 64
 Balasubramanian A., et al., 2021, *ApJ*, 914, L20
 Balasubramanian A., et al., 2022, arXiv e-prints, p. arXiv:2205.14788
 Barniol Duran R., Nakar E., Piran T., Sari R., 2015, *MNRAS*, 448, 417
 Bauswein A., Goriely S., Janka H. T., 2013, *ApJ*, 773, 78
 Bell A. R., 1978, *MNRAS*, 182, 147
 Bernuzzi S., et al., 2020, *MNRAS*, 497, 1488
 Blandford R., Eichler D., 1987, *Phys. Rep.*, 154, 1
 Blandford R. D., Ostriker J. P., 1978, *ApJ*, 221, L29
 Bykov A. M., Treumann R. A., 2011, *A&ARv*, 19, 42
 Ciolfi R., Kalinani J. V., 2020, *ApJ*, 900, L35
 Dean C., Fernández R., Metzger B. D., 2021, *ApJ*, 921, 161
 Fernández R., Metzger B. D., 2016, *Annual Review of Nuclear and Particle Science*, 66, 23
 Fong W., et al., 2019, *ApJ*, 883, L1
 Fujibayashi S., Kiuchi K., Wanajo S., Kyutoku K., Sekiguchi Y., Shibata M., 2022, arXiv e-prints, p. arXiv:2205.05557
 Guzman F. S., Lora-Clavijo F. D., Morales M. D., 2012, arXiv e-prints, p. arXiv:1212.1421
 Hajela A., et al., 2019, *ApJ*, 886, L17
 Hajela A., et al., 2022, *ApJ*, 927, L17
 Ishii A., Shigezawa T., Tanaka M., 2018, *ApJ*, 861, 25
 Kathirgamaraju A., Giannios D., Beniamini P., 2019, *MNRAS*, 487, 3914
 Krymskii G. F., 1977, *Soviet Physics Doklady*, 22, 327
 Lamb G. P., et al., 2019, *ApJ*, 870, L15
 Li L.-X., Paczyński B., 1998, *ApJ*, 507, L59
 Makhathini S., et al., 2020, arXiv e-prints, p. arXiv:2006.02382
 Martí J. M., Müller E., 2003, *Living Reviews in Relativity*, 6, 7
 Mészáros P., 2002, *ARA&A*, 40, 137
 Metzger B. D., 2017, arXiv e-prints, p. arXiv:1710.05931
 Mooley K. P., et al., 2018, *Nature*, 561, 355
 Nakar E., 2007, *Phys. Rep.*, 442, 166
 Nakar E., Piran T., 2011, *Nature*, 478, 82
 Nakar E., Piran T., 2020, arXiv e-prints, p. arXiv:2005.01754
 Nedora V., Radice D., Bernuzzi S., Perego A., Daszuta B., Endrizzi A., Prakash A., Schianchi F., 2021a, *MNRAS*, 506, 5908
 Nedora V., et al., 2021b, *ApJ*, 906, 98
 Nicholl M., et al., 2017, *ApJ*, 848, L18
 O'Connor B., Troja E., 2022, GRB Coordinates Network, 32065, 1
 Piran T., 2004, *Reviews of Modern Physics*, 76, 1143

- Radice D., Perego A., Hotokezaka K., Fromm S. A., Bernuzzi S., Roberts L. F., 2018, *ApJ*, 869, 130
 Radice D., Bernuzzi S., Perego A., 2020, *Annual Review of Nuclear and Particle Science*, 70, 95
 Rosswog S., Diener P., Torsello F., 2022, *Symmetry*, 14, 1280
 Rybicki G. B., Lightman A. P., 1979, *Radiative processes in astrophysics*
 Sedov L. I., 1946, *Journal of Applied Mathematics and Mechanics*, 10, 241
 Shibata M., Hotokezaka K., 2019, *Annual Review of Nuclear and Particle Science*, 69, 41
 Sironi L., Spitkovsky A., Arons J., 2013, *ApJ*, 771, 54
 Synge J. L., 1957, *The relativistic gas*
 Taylor G., 1950, *Proceedings of the Royal Society of London Series A*, 201, 159
 Troja E., et al., 2019, *MNRAS*, 489, 1919
 Troja E., et al., 2020, *MNRAS*, 498, 5643
 Troja E., et al., 2021, arXiv e-prints, p. arXiv:2104.13378
 Troja E., et al., 2022, *MNRAS*, 510, 1902
 Waxman E., 2006, *Plasma Physics and Controlled Fusion*, 48, B137
 Waxman E., Ofek E. O., Kushnir D., Gal-Yam A., 2018, *MNRAS*, 481, 3423

APPENDIX A: POWER-LAW APPROXIMATIONS

The $(\gamma\beta)^{\lambda}$ power-law approximations used for the derivation of the non-thermal specific flux produced by the fast tail in Eqs. (27-29) are (accurate to 10% for $0.3 < \gamma\beta < 2.5$)

$$v_c \propto \frac{(1.5 - \sqrt{2\beta^2 + 0.25})}{\gamma^{\frac{1}{2}}(\gamma - 1)^{\frac{3}{2}}} \approx (\gamma\beta)^{-3.9}, \quad (\text{A1})$$

$$L_{\nu}(v > v_c) \propto \frac{(\gamma - 1)^{(p+2)/2} \gamma^{\frac{3-p}{2}} \beta^3}{(1.5 - \sqrt{2\beta^2 + 0.25})^{\frac{p+4}{2}}} \approx 7.7(1.25 - 0.35p)(\gamma\beta)^{2.5p+2}, \quad (\text{A2})$$

$$L_{\nu}(v < v_c) \propto \frac{(\gamma - 1)^{(p+3.5)/2} \gamma^{\frac{3.5-p}{2}} \beta^3}{(1.5 - \sqrt{2\beta^2 + 0.25})^{\frac{p+5}{2}}} \approx 7.7(1.25 - 0.35p)(\gamma\beta)^{2.5p+4}. \quad (\text{A3})$$

The $(\gamma\beta)^{\lambda}$ power-law approximations used for the derivation of the non-thermal specific flux produced by the slower part of the ejecta in Eqs. (36-38) are (accurate to 10% for $0.1 < \gamma\beta < 0.7$)

$$v_c \propto \frac{(1.5 - \sqrt{2\beta^2 + 0.25})}{\gamma^{\frac{1}{2}}(\gamma - 1)^{\frac{3}{2}}} \propto (\gamma\beta)^{-3.3}, \quad (\text{A4})$$

$$L_{\nu}(v > v_c) \propto \frac{(\gamma - 1)^{(p+2)/2} \gamma^{\frac{3-p}{2}} \beta^3}{(1.5 - \sqrt{2\beta^2 + 0.25})^{\frac{p+4}{2}}} \propto (\gamma\beta)^{2.5p+0.6}, \quad (\text{A5})$$

$$L_{\nu}(v < v_c) \propto \frac{(\gamma - 1)^{(p+3.5)/2} \gamma^{\frac{3.5-p}{2}} \beta^3}{(1.5 - \sqrt{2\beta^2 + 0.25})^{\frac{p+5}{2}}} \propto (\gamma\beta)^{2.5p+2.2}. \quad (\text{A6})$$

This paper has been typeset from a $\text{\TeX}/\text{\LaTeX}$ file prepared by the author.